(Received 12 January 2026, Accepted 26 Februray 2026, Scheduled 9 April 2026)

A Universal Equivalent Thermal Network Model for PMV Machine with Detailed In-Slot Mesh

Yuxiao Wang[1,2], Zhengmeng Liu[1,2,*], Hao Ke[1,2], Qian Chen[1,2], and Guohai Liu[1,2]

[1]School of Electrical and Information Engineering, Jiangsu University, Zhenjiang 212013, China
[2]Jiangsu Key Laboratory of Drive and Intelligent Control for Electric Vehicle, Zhenjiang 212013, China

ABSTRACT: This paper proposes a novel equivalent thermal network (ETN) model for permanent magnet vernier (PMV) machines, featuring a detailed in-slot mesh to address the challenges in analyzing the temperature distribution within the slot. The key innovation is the equivalent analytical mesh, which is the equivalent mesh derived through analytical methods. First, a systematic in-slot mesh partitioning method is presented to solve the temperature distribution in the slot. This method includes a detailed mathematical derivation and implementation process. The novel mesh provides a high computational accuracy while maintaining uniform modeling requirements. Second, an accelerated solution framework combining a lumped parameter thermal network (LPTN) with ETN topology is introduced. This hybrid approach significantly reduces both computational time and modeling complexity for temperature field analysis. Finally, thermal testing was conducted on a prototype PMV machine. The accuracy of the proposed ETN model was validated by comparison with both computational fluid dynamics (CFD) simulations and experimental measurements.

1. INTRODUCTION

In recent years, permanent magnet vernier (PMV) machines have gained widespread adoption in applications such as aerospace systems [1], electric vehicle drives [2], and marine propulsion [3] owing to their high torque density, high efficiency, and superior dynamic performance. However, owing to the magnetic gear effect, PMV machines produce a significantly higher spatial harmonic content in the air-gap magnetic field than conventional permanent magnet machines. Consequently, increased high-frequency eddy-current losses and hysteresis losses were induced in the iron core. Furthermore, PMV machines typically operate with higher armature currents, a practice that considerably increases copper losses in the winding. Consequently, accurate thermal analysis, particularly transient thermal modeling to capture dynamic operational conditions, is essential during the design phase of PMV machines [4–6].

It should be noted that many existing thermal analysis methods have a trade-off between computational efficiency and accuracy. Although simplified modeling approaches can reduce simulation time, they often sacrifice fidelity owing to the excessive simplification of physical models.

Lumped parameter thermal network (LPTN) is a classical approach among the thermal modeling methodologies [7–10]. Based on simplified thermal circuits derived from mechanical structures, LPTN can be rapidly modeled and characterized by a global thermal system using a limited set of macroscopic nodes interconnected by thermal resistances and capacitances. In [11], the LPTN results correlated well with the finite element analysis (FEA), supporting its practical feasibility. However, because each node in the LPTN only provides a regional average temperature, this method is unable to accurately predict the local peak temperatures or thermal gradients [12], limiting its application for detailed thermal distribution, which is especially critical under transient conditions, where thermal gradients vary rapidly.

To overcome these limitations, the equivalent thermal network (ETN) method has been developed as an evolution of the LPTN [13–16]. Although both are reduced-order modeling methodologies, their fundamental approaches differ. The LPTN is based on a macroscopic nodal representation, in contrast to the ETN, which utilizes refined mesh discretization to form a distributed parameter network. Similar to FEA, the ETN approach discretizes parts of a permanent magnet machine into elementary units, such as T-grids, π-grids, and cross-shaped grids. This allows the ETN to characterize the local thermal distribution more accurately while maintaining relatively high computational efficiency, making it particularly suitable for transient thermal solutions, where both computational speed and spatial accuracy are required. By solving the time-dependent heat balance equations for each node, more precise transient temperature distributions can be obtained.

Nevertheless, existing ETN methods remain constrained by their limited ability to accurately resolve in-slot thermal gradient distributions. While preserving computational efficiency in transient simulations, enhancing the fidelity of in-slot modeling has become a crucial research direction for improving the practicality and predictive accuracy of ETN approaches.

At the high-fidelity end of the spectrum, computational fluid dynamics (CFD) provides detailed thermal-fluid characterization [17]; however, its prohibitive computational cost, which is especially pronounced in transient analyses involving itera-

* Corresponding author: Zhengmeng Liu (lzm@ujs.edu.cn).

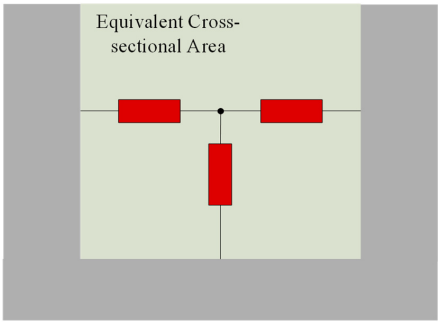

FIGURE 1. Conventional ETN in-slot model.

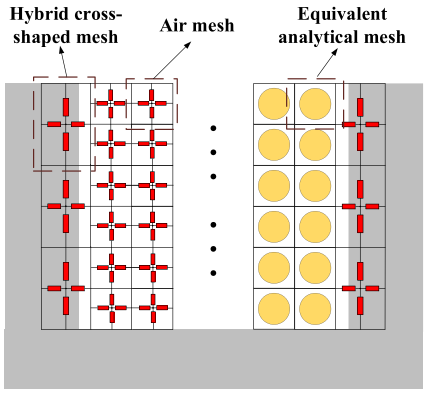

FIGURE 2. Proposed ETN in-slot model.

tive time-stepping, restricts its applicability in design-oriented studies requiring rapid iteration.

Conversely, methods prioritizing computational speed often rely on simplifications that sacrifice accuracy. Typical approaches include treating in-slot regions as homogeneous bodies with equivalent thermal properties [18], or modeling windings as copper with equivalent insulation, which are schemes that fail to capture steep thermal gradients under dynamic conditions [19, 20].

Several advanced methods have been proposed to bridge the gap between fidelity and efficiency. For instance, the novel thermal path design introduced in [21] divides the slot into distinct regions using highly conductive materials, enabling a more accurate equivalent thermal resistance evaluation within an LPTN framework. Meanwhile, analytical and subdomain-based techniques [22, 23] efficiently resolve in-slot temperature gradients through rigorous mathematical modeling, achieving high solving speed and accuracy, although their applicability remains limited by their dependence on specific slot parameters. Similarly, an enhanced 3D subdomain method [24] maintains accuracy with improved computational speed, yet still relies on homogenized slot representations.

Given these limitations, there remains a clear need for a winding modeling method that effectively balances computational speed, accuracy, and broad applicability to advance transient thermal design in PMV machines.

This paper proposes a novel ETN modeling approach for the accurate calculation of the winding temperature gradient within machine slots. An innovative equivalent in-slot mesh was developed, and its adaptability to various slot geometries was enhanced through parametric modeling. This strategy offers a high-precision tool for transient thermal management design. Section 2 details the derivation and development of an analytical in-slot mesh model. Section 3 presents a comprehensive overview of the overall ETN modeling process and unified transient-solving framework for a PMV machine. The proposed model is validated in Section 4 through comparisons with the CFD simulations and experimental measurements. The conclusions are summarized in Section 5.

2. PROPOSED IN-SLOT MESH MODEL

The in-slot region constitutes a heterogeneous structure comprising multiple components, including air, insulation materials, and copper conductors. As a result, the temperature distribution within the slot exhibited strong spatial non-uniformity. As illustrated in Fig. 1, conventional ETN in-slot modeling strategies, which often rely on equivalent cross-sectional area methods, can only estimate a single average temperature for the entire slot. Such simplistic approximations are inadequate for accurately predicting local hot-spot temperatures or capturing critical thermal gradients.

To address this limitation, this section introduces a refined in-slot thermal modeling methodology. In contrast to conventional approaches, the proposed method explicitly represents each individual winding wire and the surrounding air inside the slot as separate thermal elements. The modeling framework employs a multi-zone heterogeneous mesh strategy: a hybrid cross-shaped mesh is implemented at the core-air interface to accurately characterize the thermal interaction at the boundary; each conductor is discretized with an equivalent analytical mesh to resolve internal and surface heat conduction; and the interstitial air regions between wires are populated with dedicated air meshes to represent thermal conduction pathways. As shown in Fig. 2, which illustrates the complete thermal network along with detailed zonal mesh arrangements, the model maintains the geometric topology of the winding layout while capturing discrete heat transfer between all conductors and air domains, thereby providing a clear elucidation of the complex thermal coupling mechanisms within the slot.

This detailed winding modeling approach accounts for the complex thermal interactions within the slot. Furthermore, we recognize that the stator core is typically fabricated from laminated silicon steel sheets, which results in a highly anisotropic thermal conductivity, with the axial value being over an order of magnitude lower than the in-plane values owing to the thermal resistance of the interlaminar insulation [25]. The equivalent axial thermal conductivity was calculated as follows:

$$\frac{1}{k_{axial}} = \frac{1 - SF}{k_{air}} + \frac{SF}{k_{iron}} \tag{1}$$

where SF represents the stacking factor, and k_{iron} and k_{air} denote the thermal conductivities of iron and air, respectively.

The temperature distribution within the stator and slot is highly complex and substantially affects the computational accuracy. This complexity necessitates the development of a three-dimensional thermal network model. As illustrated in

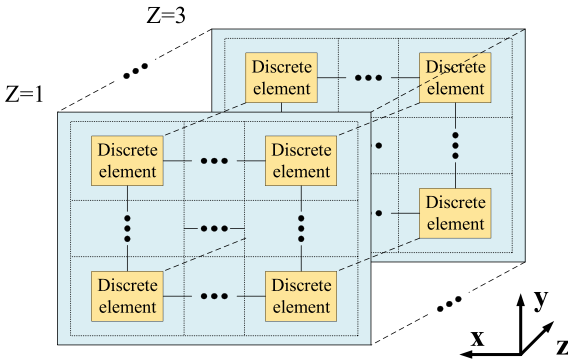

FIGURE 3. Three-dimensional topology of stator.

Fig. 3, the stator is segmented into three axial layers to accurately resolve the axial temperature gradients, whereas the axial temperature variations in the remainder of the machine are neglected to maintain computational efficiency. The model employs three-dimensional volumetric elements to discretize each material region, enabling the detailed characterization of heat transfer in all three spatial dimensions while preserving geometric fidelity. A detailed derivation of the mesh modeling methodology for the stator region is provided in the following section.

2.1. Establishment of the Equivalent Analytical Mesh

The schematic in Fig. 4 illustrates the structure of an equivalent analytical mesh. This mesh was divided into three distinct regions based on the material composition: a pure copper conductor, an insulation layer, and surface air. The following section details the derivation of the equivalent thermal resistance model for each of the three regions.

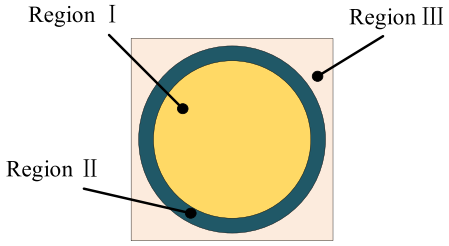

FIGURE 4. The topography of equivalent analytical mesh.

Region I:

The topology of a pure copper conductor can be equivalently represented as a long straight cylinder with uniformly distributed heat generation and isotropic thermal conductivity, where the axial length is significantly greater than its radius. Given the evident radial symmetry of the cylinder, the thermal model can be simplified into a one-dimensional heat transfer model in cylindrical coordinates along the radial direction. Therefore, the thermal resistance can be expressed as

$$\frac{1}{r}\frac{d}{dr}\left(r\frac{dT_1}{dr}\right)+\frac{P}{\pi r_1^2 L_d k_1}=0 \tag{2}$$

where P is the copper loss generated in a single conductor; r_1 is the radius of the conductor; L_d is the axial length; and k_1 is the thermal conductivity of the copper. The substitution of Equation (2) followed by integration leads to Equation (3).

$$\begin{cases} \frac{dT_1}{dr}=-\left(\frac{P}{2\pi r_1^2 L_d k_1}\right)r+\frac{C_1}{r} \\ \frac{dT_1}{dr}\big|_{r=0}=0 \end{cases} \tag{3}$$

To satisfy the boundary condition at $r=0$ in (3), the coefficient C_1 must be zero to avoid singularity. Integrating the differential equation yields (4).

$$T_1(r)=-\left(\frac{P}{4\pi r^2 L_d k_1}\right)r^2+C_2 \tag{4}$$

Applying the boundary condition $T_1(0)=T_0$ allows integration constant C_2 to be determined as T_0. Using this result, the equivalent thermal resistance for Region I was derived as follows:

$$R_1=\frac{T_1(0)-T_1(r_1)}{P}=\frac{1}{4\pi L_d k_1} \tag{5}$$

Region II:

The insulating layer can be represented as an infinitely long coaxial cylindrical shell with a topological structure analogous to a long straight torus defined by the inner radius r_1 and the outer radius r_2. The axial length of this shell is assumed to be significantly greater than the outer radius. The insulating material exhibited isotropic thermal conductivity, resulting in a constant thermal resistance in the radial, tangential, and axial directions. Similar to Region I, thermal analysis can be simplified using a one-dimensional heat transfer model in cylindrical coordinates along the radial direction. The thermal resistance equation is given by (6). The integration of (6) yields (7).

$$\frac{1}{r}\frac{d}{dr}\left(r\frac{dT_2}{dr}\right)=0 \tag{6}$$

$$T_2(r)=C_3\ln r+C_4 \tag{7}$$

As shown in Fig. 4, the geometry at the interface $(r=r_1)$ between Regions I and II requires that the temperature distribution and heat flux be continuous, and the corresponding boundary conditions can be expressed as follows:

$$\begin{cases} T_2(r_1)=T_1(r_1) \\ k_1\frac{dT_1}{dr}\big|_{r=r_1}=k_2\frac{dT_2}{dr}\big|_{r=r_1} \end{cases} \tag{8}$$

The temperature distribution of the outer layer is obtained by substituting (6):

$$T_2(r)=T_1(r_1)-\frac{P}{2\pi r_1^2 L_d k_2}r_1^2\ln\left(\frac{r}{r_1}\right) \tag{9}$$

where k_2 denotes the thermal conductivity of the insulating layer.

Subsequently, the expression for the equivalent thermal resistance in Region II is derived as

$$R_2=\frac{T_2(r_1)-T_2(r_2)}{P}=\frac{1}{2\pi L_d k_2}\ln\left(\frac{r_2}{r_1}\right) \tag{10}$$

Region III:

The surface air region was modeled as a square region with the concentric circular volume removed. The axial length of this structure was significantly larger than the side length of the square. The equivalent thermal resistance of the resulting air layer was calculated by analyzing the conductive heat transfer through it using the shape factor method [23]. The conductive heat flow between the two isothermal surfaces is given by

$$P = k_3 S[T_3 - T_2(r_2)] \tag{11}$$

where S is the shape factor governed by the geometry of the region, and k_3 denotes the thermal conductivity of the air. For the specific case of a concentric circular cavity within a square region, the shape factor is given by

$$S = \frac{2\pi L_d}{\ln\left(1.08\frac{b}{2r_2}\right)} \tag{12}$$

where b is the side length of the mesh. Substituting (12) into (10) yields the equivalent thermal resistance.

$$R_3 = \frac{T_3 - T_2(r_2)}{P} = \frac{\ln\left(1.08\frac{b}{2r_2}\right)}{2\pi L_d k_3} \tag{13}$$

As illustrated in Fig. 5(a), the thermal network topology encompasses three main heat flow directions: radial, tangential, and axial. The mesh was characterized by equivalent thermal resistances along each of these directional paths to comprehensively capture the three-dimensional heat transfer behavior.

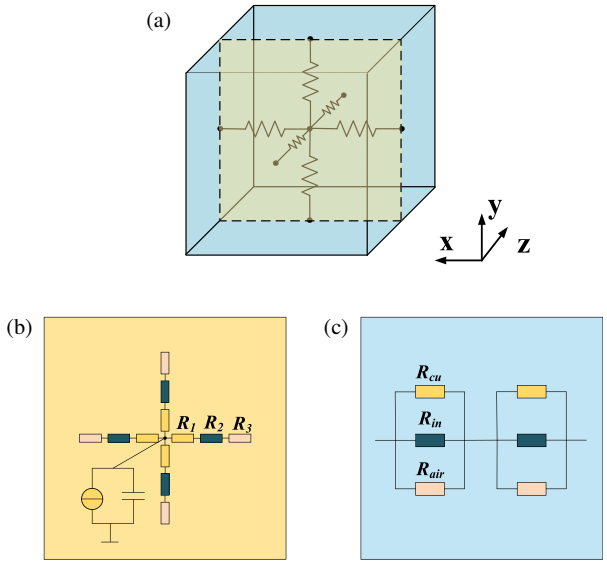

FIGURE 5. Basic mesh element. (a) Topology of mesh element. (b) X-Y plane. (c) Z direction.

For radial and tangential heat flows, as shown in Fig. 5(b), which occur through series-connected media from the winding center to its boundary, the total equivalent thermal resistance is modeled using three components: R_1 for the inner pure copper region (Region I), R_2 for the intermediate insulation layer (Region II), and R_3 for the outer air layer (Region III). Detailed analytical expressions for these radial and tangential resistances are systematically derived in the preceding sections.

Regarding the axial heat transfer, as shown in Fig. 5(c), the equivalent thermal resistance was calculated by considering the parallel combination of the three material resistances: copper, insulation, and air. The specific formulation is as follows:

$$\begin{aligned} R_{cu} &= \frac{L_s}{2\pi r_1^2 k_{cu}} \\ R_{in} &= \frac{L_s}{2\pi (r_2 - r_1)^2 k_{in}} \\ R_{air} &= \frac{L_s}{2(b^2 - \pi r_2^2) k_{air}} \\ \frac{1}{R_{axial}} &= \frac{1}{R_{cu}} + \frac{1}{R_{in}} + \frac{1}{R_{air}} \end{aligned} \tag{14}$$

where L_s is the effective thermal conductivity path length of the end winding; r_1 and r_2 are the diameter of the copper wire and insulating layer, respectively; b is the side length of the mesh; and k_{cu}, k_{in} and k_{air} are the thermal conductivities of copper, insulation and air, respectively.

To facilitate the transient thermal analysis, a heat source and thermal capacitance were assigned to the central node representing the copper wire in Region I. The total thermal capacitance of the unit is obtained by summing the heat capacities of its constituent materials: copper from Region I, insulation from Region II, and air from Region III.

Owing to the actual structural topology within the slots, the winding distribution is nonuniform, particularly near the slot edges. Consequently, a uniform mesh could not fully capture the remaining air regions. To simulate the temperature distribution accurately, both the winding and air regions require detailed discretization. A geometry-matched meshing strategy is employed to ensure mesh conformity at the interfaces. This approach maintains geometric consistency and significantly improves the computational accuracy of the thermal gradients. For mesh elements consisting of a single material, the thermal resistance was calculated directly using the standard parallel-plate formula:

$$R = \frac{L}{k_{air} A} \tag{15}$$

where k_{air} is the thermal conductivity of air; L is the length of the heat flow path; and A is the cross-sectional area perpendicular to the heat flow.

2.2. Establishment of the End Winding

The intricate configuration of the end winding and its constrained heat dissipation characteristics play a critical role in the thermal management of electric machines. To address this, an independent end winding model was introduced to replace the conventional simplified circular equivalent model. This new model is integrated with the proposed in-slot winding mesh described in Section 2.1.

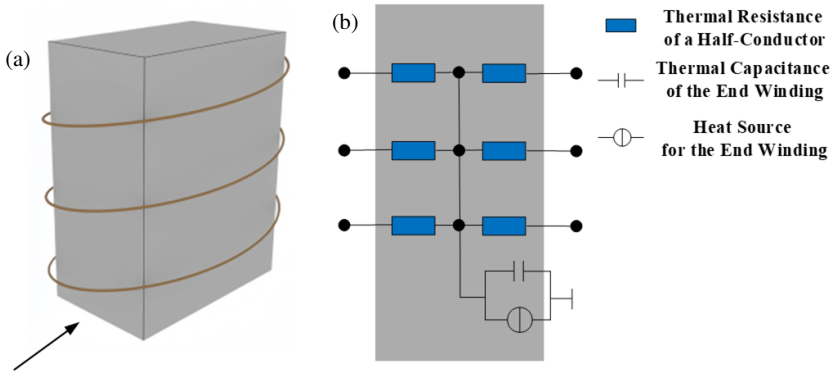

FIGURE 6. Equivalent thermal model of the end winding. (a) Schematic of the end winding. (b) Equivalent thermal model.

The end winding segment on a single side of a tooth was established as the fundamental modeling unit. This approach preserves computational efficiency by solving for the average temperature of the segment.

A detailed schematic of the proposed end winding thermal network is presented in Fig. 6. The figure illustrates the mapping from the physical conductor layout to the equivalent thermal network. The left panel shows the geometric distribution and topological connections of a representative set of conductor turns within the tooth-side space. The right panel depicts the corresponding nodal network of thermal resistances. In this model, each end-winding is divided tangentially into two discrete units. The central nodes of these units are thermally coupled, with the total heat loss and aggregate thermal capacitance of the winding assembly applied to these nodes. All thermal resistances in the network are calculated systematically based on Equation (14). The resulting nodal temperatures represent the spatially averaged temperature of the segment, preserving essential thermal paths and dynamics while maintaining computational tractability.

Owing to the high thermal resistance in the radial and tangential directions from the enclosed air inside the machine casing, their impact on the overall heat transfer was secondary. Thus, the thermal behavior in these directions is captured by representing the entire end winding unit with a single node that yields its average temperature.

Accordingly, the thermal model is implemented as follows: For the axial heat flow, the equivalent resistance was calculated by considering the parallel combination of the three material resistances: copper, insulation, and air. For the radial and tangential directions, the end winding unit is characterized by a single temperature obtained via the nodal method, effectively averaging the thermal effects without resolving the detailed, high-resistance networks.

2.3. Hybrid Cross-Shaped Mesh Elements

Figure 7(a) illustrates the hybrid cross-shaped mesh unit used for the stator tooth in the proposed ETN model. This unit was established by discretizing the geometry into distinct thermal paths. The equivalent thermal conductance of the mesh was resolved into three orthogonal components: radial (G_{r1}, G_{r2}), tangential (G_{t1}, G_{t2}), and axial (G_{a1}, G_{a2}). This modeling approach offers two main advantages. First, its increased nodal density enables more detailed local modeling, resulting in a more accurate temperature distribution. Second, the mesh can be generated in a highly uniform and flexible manner by varying several key geometric parameters.

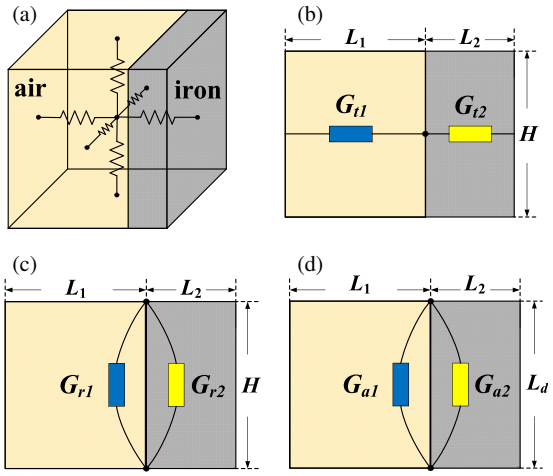

FIGURE 7. Hybrid cross-shaped mesh element. (a) Topology of mesh element. (b) Tangential direction. (c) Radial direction. (d) Axial direction.

The calculations for these conductance components are shown in Fig. 7. The model considers a cubic element with height H and width L_d containing two distinct materials: air and iron. The air segment had a length of L_1, and the iron core segment had a length of L_2. The total thermal conductance was resolved into three components: radial, tangential, and axial. The expressions for equivalent conductance in each direction are derived as follows:

$$
\begin{aligned}
G_t &= \frac{1}{\left(\frac{1}{G_{t1}} + \frac{1}{G_{t2}}\right)} = \frac{k_{air} H L_d}{\left(L_1 + L_2 \frac{k_{air}}{k_{iron}}\right)} \approx k_{air} \frac{H L_d}{L_1} \\
G_r &= G_{r1} + G_{r2} = k_{iron} \left(\frac{k_{air}}{k_{iron}} \frac{L_1 L_d}{H} + \frac{L_2 L_d}{H} \right) \\
&\approx \frac{k_{iron} L_2 L_d}{H}
\end{aligned}
\tag{16}
$$

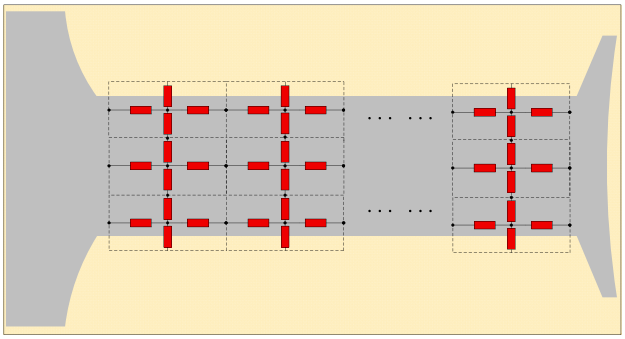

FIGURE 8. Mesh division of the hybrid cross-shaped mesh in the tooth section.

$$G_a = G_{a1} + G_{a2} = k_{iron}\left(\frac{k_{air}}{k_{iron}}\frac{L_1 H}{L_d} + \frac{L_2 H}{L_d}\right) \approx \frac{k_{iron} L_2 H}{L_d}$$

where L_d denotes the axial length. Given that the thermal conductivity of air is much lower than that of the iron core ($k_{air} \ll k_{iron}$), the equivalent conductance expressions in the radial, tangential, and axial directions can be approximated using the dominant terms on the right-hand side of the equations. Unlike conventional thermal meshes, which are composed of a single material [26], this unit is a composite of two distinct materials. Consequently, the thermal contribution of the air region can be neglected in the tangential conductance calculation, whereas the contribution of the iron core can be neglected in the radial and axial conductance calculation. This approach significantly improves the modeling efficiency by simplifying the calculations while maintaining accuracy through a geometry-aware design.

To demonstrate the advantages of the proposed hybrid cross-shaped mesh for thermal modeling, a representative scenario is presented in Fig. 8. The target tooth section typically comprises two distinct materials: iron and air. When modeling such complex geometries, conventional thermal resistance connections between different materials often introduce inaccuracies that compromise the fidelity of the temperature field simulations.

In contrast, the proposed hybrid cross-shaped mesh effectively overcame these limitations. Applied specifically to the tooth-slot junction region, it offers enhanced flexibility in mesh sizing and connectivity, preserves local modeling consistency, and reduces simulation errors arising from improper nodal connections in geometrically complex slot areas [27].

To balance accuracy and computational efficiency, the mesh parameters were tailored to the topological features of the region. A finer discretization of the teeth allows for improved thermal mapping, which is critical because the tooth temperature distribution directly affects the accuracy of adjacent winding temperature predictions. As a trade-off between accuracy and efficiency, the tooth length and width were divided into five and three segments, respectively, as shown in Fig. 8. The heat source (P) and thermal capacitance (C) were assigned to the center of each mesh cell (omitted for clarity). The heat source was applied only to the core sections, whereas the thermal capacitance was derived by superimposing contributions from both the air and iron volumes within each cell. The boundary nodes of the hybrid mesh facilitate heat exchange with the adjacent slot region mesh.

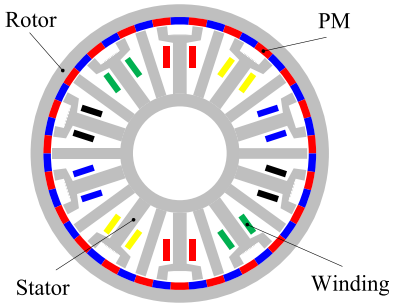

FIGURE 9. 20-slots/46-poles PMV machine.

3. SOLUTION PROCESS OF THE ETN

A 20-slot/46-pole PMV machine was selected as a case study to validate the proposed thermal modeling methods. Unlike existing PMV machines with uniformly distributed split-teeth stators, the proposed machine employs a hybrid stator tooth design to utilize multiple working harmonics, thereby achieving a high power factor, high torque density, and improved fault-tolerant capability. However, these multiple working harmonics also generate higher losses than in the original design, which can increase the operating temperature of the entire machine. Thus, an accurate thermal analysis is essential.

The cross-sectional topology of the proposed PMV machine is displayed in Fig. 9. Whereas conventional PMV machines adopt a split-teeth stator structure, the proposed design incorporates both slot-opening and split-teeth elements, forming a hybrid stator configuration. Each coil in the machine consists of 45 turns. The key machine parameters are listed in Table 1.

TABLE 1. Main parameters of the PMV machine.

Parameter	Value
Slot/Pole number	20/46
Rated speed (r/min)	600
Turns per slot	45
Axial length (mm)	60
Stator outside radial (mm)	60
Stator inner radial (mm)	22
Rotor outside radial (mm)	70
Rotor inner radial (mm)	60.5
PM thickness (mm)	3.5
Armature tooth width (deg)	6.4
Iron material	DW465-50
Permanent magnet material	NdFe35

A comprehensive thermal model of the entire machine was required to accurately calculate the transient thermal perfor-

TABLE 2. Properties of materials.

Materials	Thermal conductivity [W/(m·K)]	Density [kg/m^3]	Specific heat [J/kg]
Air	0.023	1.23	1000
Copper	385	8900	390
Wire insulation	0.26	1000	1400
Iron core (radial/tangential)	30	7650	460
Iron core (axial)	12	7650	460
PM	7.5	7400	450
Case	202	2700	900
Shaft	50	7850	480

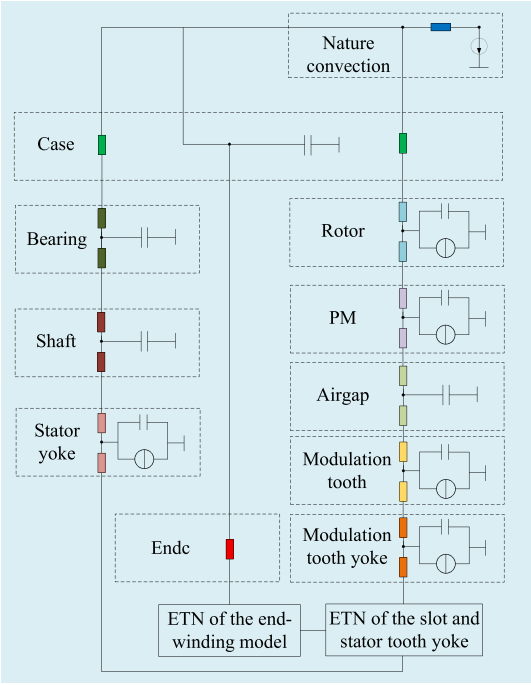

FIGURE 10. LPTN of the machine.

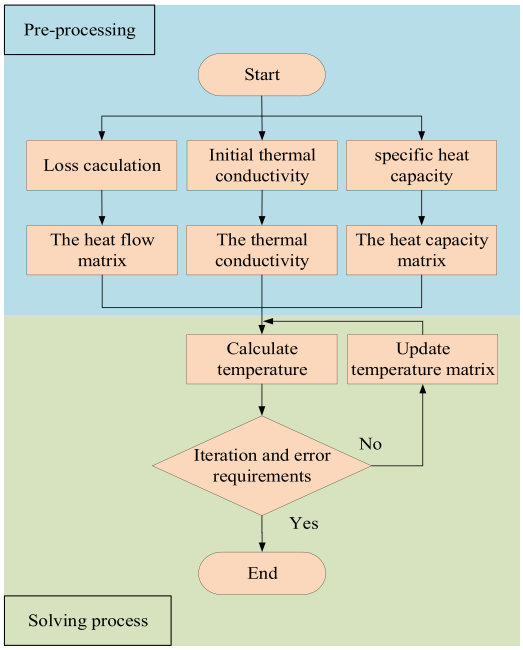

FIGURE 11. Solving process of the coupled model.

mance of the proposed PMV machine. The material properties used in the thermal model are listed in Table 2. A simplified LPTN is adopted for the machine regions outside the stator slots and teeth, whereas the tooth region and in-slot winding area are modeled using the high-fidelity strategy introduced in Section 2. As illustrated in Fig. 10, to compute the transient temperature in each region, the thermal resistance between the two nodes is divided into two halves, with a heat source and a thermal capacitance connected at the central node. The corresponding formulation is summarized in the Appendix.

The transient thermal behavior is governed by the following differential equation:

$$\frac{dT}{dt} = C^{-1}\left(P - GT\right) \tag{17}$$

where T, C, P, and G denote the nodal temperature, thermal capacitance, heat source, and thermal conductance, respectively.

As illustrated in Fig. 11, a transient solver based on the thermal network model is developed to evaluate the thermal characteristics of the PMV machine. The solution procedure is as follows. First, the initial conditions were defined, including initializing the temperature field, defining the power of the heat sources, and calculating the thermal capacitance values. The nodal temperature rise was then computed by solving the system of differential equations given in (17) using an iterative numerical method. An appropriate time step was selected for this integration. The system was considered to have reached thermal equilibrium when the rate of temperature change between consecutive iterations fell below a predefined convergence threshold. The resulting temperature-time history represents the desired transient thermal response.

4. CFD AND EXPERIMENTAL VERIFICATION

The accuracy of the proposed ETN model was validated through comparison with both CFD simulations and experimental measurements. Although conceptually analogous to the FEM in its discretization approach, the CFD framework was selected as the numerical benchmark owing to its superior fi-

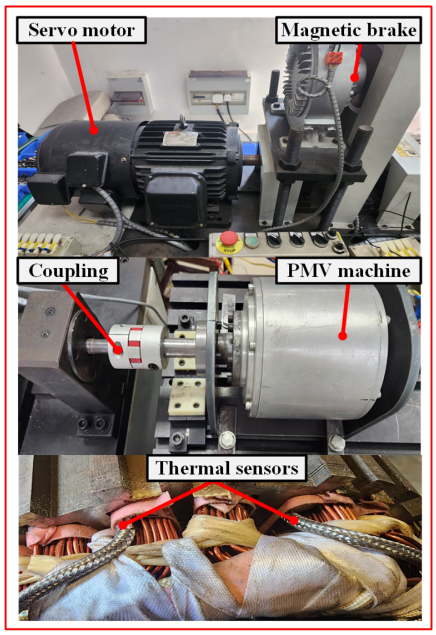

FIGURE 12. Experiment platform.

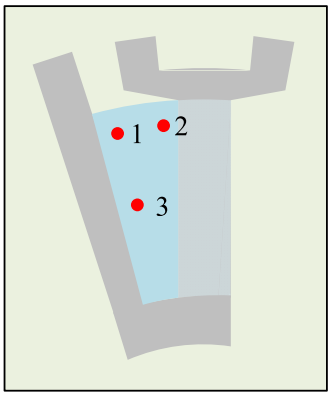

FIGURE 13. Location of the thermal sensors.

delity. The validation compares the predicted temperatures for the major components and the detailed temperature distribution within the stator slot.

Figure 12 shows the prototype experimental platform. Temperature was measured using a PT100 platinum resistance thermometer, which operates on the principle of platinum resistance temperature characteristics and provides high accuracy ($\pm 0.1°C$) and excellent long-term stability.

As shown in Fig. 13, multiple PT100 sensors were strategically placed at critical axial center locations to enable accurate multi-point temperature measurements. The configuration consists of three measurement channels: channels 1, 2, and 3 are positioned along the axial center of the slot: channel 1 in the upper-left quadrant, channel 2 in the upper-right quadrant, and channel 3 is offset to the left of the slot center. The corresponding steady-state copper and iron losses at load currents of 3 and 10 A are listed in Table 3.

Figure 14 shows the computational mesh used for the CFD simulations, including the explicit modeling of the individual

TABLE 3. Steady-state losses of machine (W).

Type	3 A	10 A
Copper loss	4.83	53.56
Iron loss	33.41	43.11
Eddy current loss	10.46	13.2
Additional losses	2.19	7.09

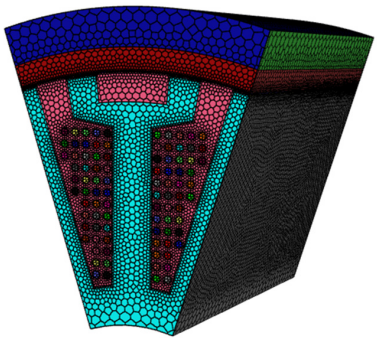

FIGURE 14. The CFD model of the proposed machine.

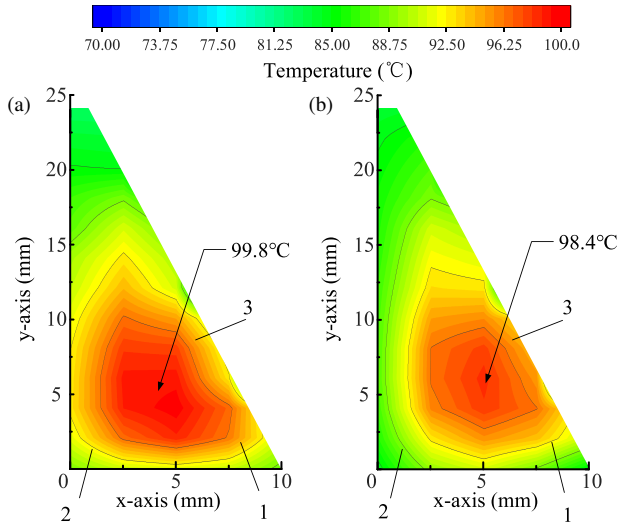

FIGURE 15. Temperature distribution in the single slot. (a) ETN model. (b) CFD solution.

winding wires. By leveraging the symmetrical structure of the machine, only the one-tenth periodic sector was modeled. The system was energized until the current reached a rated value of 10 A, and a thermal steady state was achieved.

Figure 15 compares the resulting winding temperature distributions within a single slot from the ETN and CFD models, where the points labeled 1, 2, and 3 correspond to the temperature sensor locations shown in Fig. 14. The results reveal a distinct thermal gradient across the tooth, characterized by a gradual temperature decrease from the slot center to the slot opening and a concentrated high-temperature region near the slot center. The temperature distribution of the proposed ETN model in the slot center shows good agreement with the CFD results, which is a significant improvement over the traditional ETN model. A quantitative comparison of steady-state tem-

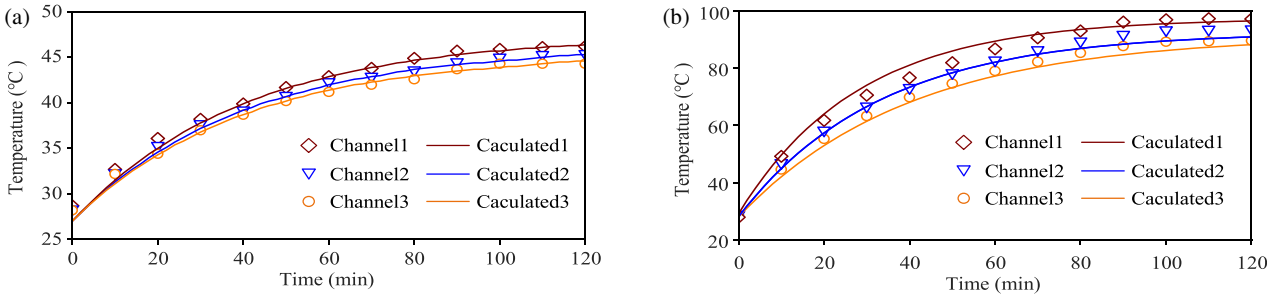

FIGURE 16. Comparison of transient temperature, (a) in 10 A, (b) in 3 A.

TABLE 4. Comparison of ETN, CFD, and experimental results (°).

Location	ETN	CFD	Experiment
1	88.3	88.6	89.7
2	91.1	89.8	93.7
3	96.6	96.1	97.3
End winding	85.2	82.9	\
PM	72.8	70.9	\
Rotor	71.7	69.5	\
Case	59.7	56.4	\

peratures is presented in Table 4. The ETN results were also in good agreement with the measured data, with all errors remaining within an acceptable range. Furthermore, a mesh refinement study confirmed that increasing the mesh density around the modulating tooth improved the agreement with the CFD results, thereby enhancing the accuracy of the model.

Figure 16(a) shows a comparison of the simulated and experimental temperature increases at the rated load. The simulation was performed by using a thermal network model with 11,849 nodes. Channel 3, located in the central slot region where the highest temperature occurs, recorded a measured value of 96.6°C. The close agreement between the simulated and measured profiles verified the accuracy and reliability of the winding model. Both sets of results show satisfactory agreement in their overall trends. The transient simulation in MATLAB required approximately 290 s (server: AMD Ryzen 9 7945HX, 2.5 GHz, 32 GB RAM).

Figure 16(b) compares the ETN results with the measured temperature data under light-load (3 A) conditions. The comparison shows that the model error under a light load is significantly smaller than that under rated conditions. This improvement was primarily because the copper and iron losses were both smaller and more uniformly distributed under a light load. The ETN model assumes a uniform mesh-based heat source distribution. Because the actual loss distribution at a light load aligns better with this theoretical assumption, the accuracy of the model is improved.

5. CONCLUSION

This study proposes a novel thermal modeling method that utilizes a detailed in-slot mesh to accurately calculate the winding temperature gradient within slots. Unlike the traditional computational fluid dynamics method, which is too time-consuming, and the conventional equivalent thermal network method, which is inaccurate, this hybrid approach retains the high efficiency of the equivalent thermal network while achieving high precision of computational fluid dynamics for analyzing the temperature in key components. Integrated with a hybrid cross-shaped mesh technique, it accurately resolves the machine's local geometry, overcoming the challenges posed by the complex distribution of the winding. The model efficiently calculates the transient temperature field and gradient distribution in a 20-slot/46-pole permanent magnet vernier machine, significantly reducing the computation time.

Comparisons with computational fluid dynamics simulations and prototype tests validated the method's dual advantages of high computational efficiency and accuracy. This standardized modeling approach enables the rapid construction of thermal models and enhances the efficiency of multi-physical field coupling analysis, such as electromagnetic-thermal studies. It should be noted that the current model assumes a uniform stator iron loss distribution, which may not fully reflect the real operating conditions. Future work will integrate a magnetic network model to calculate localized iron losses under various operating conditions and establish a bidirectional magneto-thermal coupling framework to further improve prediction accuracy.

ACKNOWLEDGEMENT

This work was supported in part by the National Natural Science Foundation of China under Grant 52377054 and the Senior Talent Fund of Jiangsu University under Grant 5501140009.

APPENDIX A.

In Fig. 10, the PMV is divided into different parts: ambient, case, rotor, PM, air gap, modulation tooth, modulation tooth yoke, winding, end winding, stator yoke, shaft, and bearing.

Under the following simplifying assumptions:

1. Heat transfer through radiation is neglected.
2. The ambient temperature is constant in 28°C.
3. Windage and friction losses are negligible.
4. The machine utilizes natural cooling.

Based on the LPTN with a total of 29 nodes for the main machine components, excluding the stator section, the primary thermal conductances between parts can be computed with sufficient accuracy using analytical equations.

R_{rotor} — Conductive thermal resistance

$$R_{rotor} = \frac{1}{4\pi k_{iron} L_r} \ln\left(\frac{r_{or}}{r_{ir}}\right) \tag{A1}$$

where k_{iron} is the thermal conduction coefficient of iron; L_r is the axial length of the rotor; r_{or} and r_{ir} are the outer and inner radii of the rotor, respectively.

R_{PM} — Conductive thermal resistance

$$R_{PM} = \frac{1}{4\pi k_{PM} L_{PM}} \ln\left(\frac{r_{oPM}}{r_{iPM}}\right) \tag{A2}$$

where k_{PM} is the thermal conduction coefficient of the PM; L_{PM} is the axial length of the PM; r_{oPM} and r_{iPM} are the outer and inner radii of the PM, respectively.

R_{air} — Conductive and convective thermal resistance

$$R_{air} = \frac{1}{2}\left(\frac{R_{aconv} R_{acond}}{R_{aconv} + R_{acond}}\right) \tag{A3}$$

where R_{acond} and R_{aconv} are the conductive and convective thermal resistances of the air gap, respectively.

$$R_{acond} = \frac{1}{2\pi k_{air} L_{air}} \ln\left(\frac{r_{oair}}{r_{iair}}\right) \tag{A4}$$

where k_{air} is the thermal conduction coefficient of air; L_{air} is the axial length of the air gap; r_{oair} and r_{iair} are the outer and inner radii of the air gap, respectively.

To calculate the convective thermal resistance, the Taylor number was first determined to determine the flow regime.

$$Ta = \frac{r_{oair}\omega^2\delta^3}{\nu^2} \tag{A5}$$

where ω is the rotor angular velocity; δ is the length of the air gap; and ν is the kinematic viscosity of the air. Based on the results of the Taylor number calculations, the flow in the air gap was determined to be stable and laminar. This flow regime was then used to calculate the convective thermal resistance.

$$R_{aconv} = \frac{\delta}{k_{air} A_{air} Nu} \tag{A6}$$

where A_{air} is the surface area of the rotor, and Nu is the Nusselt number, which is taken as 1.

R_{mt} — Conductive thermal resistance

$$R_{mt} = \frac{v_1}{4\pi k_{iron} L_{mt}} \ln\left(\frac{r_{omt}}{r_{imt}}\right) \tag{A7}$$

where v_1 is the ratio of the modulation teeth in the tip; L_{mt} is the axial length of the modulation teeth; r_{omt} and r_{imt} are the outer and inner radii of the modulation teeth, respectively.

R_{mty} — Conductive thermal resistance

$$R_{mty} = \frac{v_2}{4\pi k_{iron} L_{mty}} \ln\left(\frac{r_{omty}}{r_{imty}}\right) \tag{A8}$$

where v_2 is the ratio of the modulation teeth in the yoke; L_{mty} is the axial length of the modulation tooth yoke; r_{omty} and r_{imty} are the outer and inner radii of the modulation tooth yoke, respectively.

R_{endc} — Convective thermal resistance between end winding and case

$$R_{endc} = \frac{1}{2\pi k_{air}(L_c - L_{st})} \ln\left(\frac{r_{ost}}{r_{ost} - \alpha(r_{ost} - r_{ist})}\right) \tag{A9}$$

where L_c and L_{st} are the axial lengths of the case and stator tooth; r_{ost} and r_{ist} are the outer and inner radii of the stator tooth; α is the reduction coefficient < 1. A reasonable range of α is between 0.4 and 0.7.

R_{sy} — Conductive thermal resistance

$$R_{sy} = \frac{1}{4\pi k_{iron} L_{sy}} \ln\left(\frac{r_{osy}}{r_{isy}}\right) \tag{A10}$$

where L_{sy} is the axial length of the stator yoke, and r_{osy} and r_{isy} are the outer and inner radii of the stator yoke, respectively

R_{sh} — Conductive thermal resistance

$$R_{sh} = \frac{1}{4\pi k_{sh} L_{sh}} \ln\left(\frac{r_{osh}}{r_{ish}}\right) \tag{A11}$$

where k_{sh} is the thermal conduction coefficient of the shaft; L_{sh} is the axial length of the shaft; r_{osh} and r_{ish} are the outer and inner radii of the shaft, respectively.

R_b — Conductive thermal resistance

$$R_b = \frac{k_1(0.12 - k_2 D_b)(33 - k_3\omega D_b)}{4} \tag{A12}$$

where k_1, k_2, and k_3 are the empirical constants, $k_1 = 0.45\,\mathrm{K/W}$, $k_2 = 1\,\mathrm{m^{-1}}$, and $k_3 = 1\,\mathrm{s^{-1}}$, and D_b is the average diameter of bearing.

R_{cr} — Conductive thermal resistance between case and rotor

$$R_{cr} = \frac{1}{2\pi k_c L_c} \ln\left(\frac{r_{oc}}{r_{ic}}\right) + \frac{1}{2\pi k_{air} L_s} \ln\left(\frac{r_{oy} + g}{r_{oy}}\right) \tag{A13}$$

where k_c is the thermal conduction coefficient of the case; L_c is the axial length of the case; r_{oc} and r_{ic} are the outer and inner radii of the case, respectively; and g is the effective contact gap between the case and yoke.

R_{cb} — Conductive thermal resistance between case and bearing

$$R_{cb} = \frac{L_c}{2\pi k_c r_{ac}^2} \tag{A14}$$

where r_{ac} denotes the average radius of the case.

The additional loss was defined as 0.5% of the motor output power.

$$P_{add} = \frac{2\pi}{60} T \times n \times 0.005 \tag{A15}$$

where T is the torque in N·m, and n is the speed in r/min. Additional losses were allocated to the core regions in proportion to their volume.

REFERENCES

[1] Ullah, S., S. P. McDonald, R. Martin, M. Benarous, and G. J. Atkinson, "A permanent magnet assist, segmented rotor, switched reluctance drive for fault tolerant aerospace applications," *IEEE Transactions on Industry Applications*, Vol. 55, No. 1, 298–305, Jan.-Feb. 2019.

[2] Li, Q., S. Liu, W. Fang, X. Li, and Z. Tse, "Sideband vibration suppression of interior permanent magnet synchronous motors for electric vehicles under multiple operating conditions," *IEEE Transactions on Transportation Electrification*, Vol. 9, No. 1, 322–335, Mar. 2023.

[3] Wang, M., C. Tong, Z. Song, J. Liu, and P. Zheng, "Performance analysis of an axial magnetic-field-modulated brushless double-rotor machine for hybrid electric vehicles," *IEEE Transactions on Industrial Electronics*, Vol. 66, No. 1, 806–817, Jan. 2019.

[4] Zhao, W., K. Du, and L. Xu, "Design considerations of fault-tolerant permanent magnet vernier machine," *IEEE Transactions on Industrial Electronics*, Vol. 67, No. 9, 7290–7300, Sep. 2020.

[5] Du, K., Z. Liu, W. Yan, L. Xu, and G. Liu, "Analysis of fault-tolerant permanent magnet vernier machines with improved output torque," *IEEE Transactions on Energy Conversion*, Vol. 40, No. 2, 1434–1444, Jun. 2025.

[6] Du, K., L. Xu, W. Zhao, and G. Liu, "Analysis and design of a fault-tolerant permanent magnet vernier machine with improved power factor," *IEEE Transactions on Industrial Electronics*, Vol. 69, No. 5, 4353–4363, May 2022.

[7] Zhu, S., M. Cheng, and X. Cai, "Direct coupling method for coupled field-circuit thermal model of electrical machines," *IEEE Transactions on Energy Conversion*, Vol. 33, No. 2, 473–482, Jun. 2018.

[8] Liang, D., Z. Q. Zhu, P. Wang, and Y. Chen, "Identification of thermal parameters for PMSMs based on high-fidelity lumped-parameter thermal model," *IEEE Transactions on Transportation Electrification*, Vol. 11, No. 4, 9483–9496, 2025.

[9] Burke, R., A. Giedymin, Z. Wu, H. Chuan, N. Bourne, and J. G. Hawley, "A lumped parameter thermal model for single-sided AFPM machines with experimental validation," *IEEE Transactions on Transportation Electrification*, Vol. 6, No. 3, 1065–1083, Sep. 2020.

[10] Boglietti, A., M. Cossale, M. Popescu, and D. A. Staton, "Electrical machines thermal model: Advanced calibration techniques," *IEEE Transactions on Industry Applications*, Vol. 55, No. 3, 2620–2628, May-Jun. 2019.

[11] Nategh, S., H. Zhang, O. Wallmark, A. Boglietti, T. Nassen, and M. Bazant, "Transient thermal modeling and analysis of railway traction motors," *IEEE Transactions on Industrial Electronics*, Vol. 66, No. 1, 79–89, Jan. 2019.

[12] Wallscheid, O. and J. Böcker, "Global identification of a low-order lumped-parameter thermal network for permanent magnet synchronous motors," *IEEE Transactions on Energy Conversion*, Vol. 31, No. 1, 354–365, Mar. 2016.

[13] Cao, D., W. Zhao, J. Ji, L. Ding, and J. Zheng, "A generalized equivalent magnetic network modeling method for vehicular dual-permanent-magnet vernier machines," *IEEE Transactions on Energy Conversion*, Vol. 34, No. 4, 1950–1962, Dec. 2019.

[14] Romanazzi, P., V. Galizzi, F. Carbone, A. Miotto, and D. A. Howey, "Improved thermal equivalent circuit element applied to an external rotor SPM machine," in *2016 XXII International Conference on Electrical Machines (ICEM)*, 2718–2724, Lausanne, Switzerland, Sep. 2016.

[15] Liang, D., Z. Q. Zhu, R. Nilifard, Z. Azar, and N. Madani, "Novel high-order lumped-parameter thermal models for predicting spatial temperature distribution in electrical machines," *IEEE Transactions on Transportation Electrification*, Vol. 11, No. 2, 6675–6689, Apr. 2025.

[16] Zhu, X., Z. Yang, J. Wu, Z. Xiang, S. Liu, Y. Chen, and L. Quan, "Multiphysics dimension-reduced optimization of a PM hub motor based on electromagnetic-thermal mesh-shared network model," *IEEE Transactions on Transportation Electrification*, Vol. 11, No. 1, 4586–4597, Feb. 2025.

[17] Fan, X., R. Qu, J. Li, D. Li, B. Zhang, and C. Wang, "Ventilation and thermal improvement of radial forced air-cooled FSCW permanent magnet synchronous wind generators," *IEEE Transactions on Industry Applications*, Vol. 53, No. 4, 3447–3456, Jul.-Aug. 2017.

[18] Idoughi, L., X. Mininger, F. Bouillault, L. Bernard, and E. Hoang, "Thermal model with winding homogenization and FIT discretization for stator slot," *IEEE Transactions on Magnetics*, Vol. 47, No. 12, 4822–4826, Dec. 2011.

[19] Boglietti, A., E. Carpaneto, M. Cossale, and S. Vaschetto, "Stator-winding thermal models for short-time thermal transients: Definition and validation," *IEEE Transactions on Industrial Electronics*, Vol. 63, No. 5, 2713–2721, May 2016.

[20] Boglietti, A., M. Cossale, S. Vaschetto, and T. Dutra, "Thermal conductivity evaluation of fractional-slot concentrated-winding machines," *IEEE Transactions on Industry Applications*, Vol. 53, No. 3, 2059–2065, May-Jun. 2017.

[21] Hebala, A., P. H. Connor, S. Nuzzo, C. Gerada, and M. Galea, "A holistic analysis and experimental testing of a passive heat path for electric motors slots," *IEEE Transactions on Transportation Electrification*, Vol. 11, No. 3, 8128–8138, Jun. 2025.

[22] Fan, X., D. Li, R. Qu, and C. Wang, "A dynamic multilayer winding thermal model for electrical machines with concentrated windings," *IEEE Transactions on Industrial Electronics*, Vol. 66, No. 8, 6189–6199, Aug. 2019.

[23] Zhao, W., D. Cao, J. Ji, L. Huang, and T. Liu, "A generalized mesh-based thermal network model for SPM machines combining coupled winding solution," *IEEE Transactions on Industrial Electronics*, Vol. 68, No. 1, 116–127, 2021.

[24] Liu, J., X. Wang, W. Zhao, Z. Xing, and H. Zhou, "An upgraded hybrid subdomain method toward three-dimensional thermal performance of synchronous reluctance motor," *International Journal of Thermal Sciences*, Vol. 220, 110284, 2026.

[25] Boglietti, A., A. Cavagnino, D. Staton, M. Shanel, M. Mueller, and C. Mejuto, "Evolution and modern approaches for thermal analysis of electrical machines," *IEEE Transactions on Industrial Electronics*, Vol. 56, No. 3, 871–882, Mar. 2009.

[26] Anteby, I. and I. Shai, "Modified conduction shape factors for isothermal bodies embedded in a semi-infinite medium," *Numerical Heat Transfer, Part A: Applications*, Vol. 23, No. 2, 233–245, 1993.

[27] Ke, H., Z. Liu, Q. Chen, G. Liu, and G. Xu, "Analysis of a spoke-type ferrite PM motor with assisted poles based on equivalent magnetic network with hybrid cross-shaped mesh elements," *IET Electric Power Applications*, Vol. 17, No. 4, 474–486, Apr. 2023.